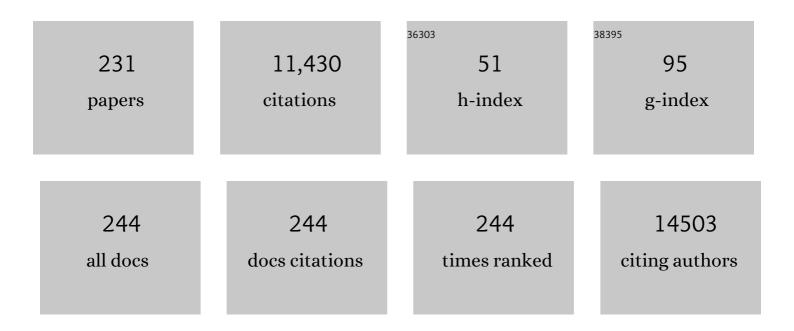
Yang Shen

List of Publications by Year in descending order

Source: https://exaly.com/author-pdf/3074946/publications.pdf Version: 2024-02-01



#	Article	IF	CITATIONS
1	Comparison of the Effects of Temperature and Dehydration Mode on Glycerin-Based Approaches to SMILE-Derived Lenticule Preservation. Cornea, 2022, 41, 470-477.	1.7	8
2	Highly Sensitive Strain Sensor from Topological‧tructure Modulated Dielectric Elastic Nanocomposites. Advanced Materials Technologies, 2022, 7, 2101190.	5.8	5
3	Predictive factors of the accelerated transepithelial corneal cross-linking outcomes in keratoconus. BMC Ophthalmology, 2022, 22, 7.	1.4	2
4	Image-Based Regulation of Mobile Robots Without Pose Measurements. , 2022, 6, 2156-2161.		2
5	China's Terrestrial Carbon Sink Over 2010–2015 Constrained by Satellite Observations of Atmospheric CO ₂ and Land Surface Variables. Journal of Geophysical Research G: Biogeosciences, 2022, 127, .	3.0	8
6	Prediction of Refractive Error Based on Ultrawide Field Images With Deep Learning Models in Myopia Patients. Frontiers in Medicine, 2022, 9, 834281.	2.6	3
7	Optical Vector Vortex Generation by Spherulites with Cylindrical Anisotropy. Nano Letters, 2022, 22, 2444-2449.	9.1	5
8	Concurrently enhanced mechanical properties and capacitive performance in all-organic dielectric polymer blend via phase separation. Journal of Applied Physics, 2022, 131, .	2.5	3
9	Anthropogenic emissions estimated using surface observations and their impacts on PM2.5 source apportionment over the Yangtze River Delta, China. Science of the Total Environment, 2022, 828, 154522.	8.0	9
10	An Optical/Ferroelectric Multiplexing Multidimensional Nonvolatile Memory from Ferroelectric Polymer. Advanced Materials, 2022, 34, e2202181.	21.0	15
11	Spectral Thermal Spreading Resistance of Wide-Bandgap Semiconductors in Ballistic-Diffusive Regime. IEEE Transactions on Electron Devices, 2022, 69, 3047-3054.	3.0	13
12	An Improved Earthquake Catalog During the 2018 KıÌ,,lauea Eruption From Combined Onshore and Offshore Seismic Arrays. Earth and Space Science, 2022, 9, .	2.6	2
13	Excellent Stability in Polyetherimide/SiO ₂ Nanocomposites with Ultrahigh Energy Density and Discharge Efficiency at High Temperature. Small, 2022, 18, .	10.0	54
14	Explainable Deep Relational Networks for Predicting Compound–Protein Affinities and Contacts. Journal of Chemical Information and Modeling, 2021, 61, 46-66.	5.4	30
15	Structural basis for recognition of bacterial cell wall teichoic acid by pseudo-symmetric SH3b-like repeats of a viral peptidoglycan hydrolase. Chemical Science, 2021, 12, 576-589.	7.4	11
16	Impact of weather and emission changes on NO2 concentrations in China during 2014–2019. Environmental Pollution, 2021, 269, 116163.	7.5	39
17	TALE: Transformer-based protein function Annotation with joint sequence–Label Embedding. Bioinformatics, 2021, 37, 2825-2833.	4.1	52
18	Identification and Engagement of Passive Subjects in Multiparty Conversations by a Humanoid Robot. , 2021, , .		3

#	Article	IF	CITATIONS
19	C4+ Surrogate Models for Thermophysical Properties of Aviation Kerosene RP-3 at Supercritical Pressures. Energy & Fuels, 2021, 35, 7858-7865.	5.1	7
20	Sensor Reduction, Estimation, and Control of an Upper-Limb Exoskeleton. IEEE Robotics and Automation Letters, 2021, 6, 1012-1019.	5.1	15
21	Array-Based Convolutional Neural Networks for Automatic Detection and 4D Localization of Earthquakes in Hawaiâ€~i. Seismological Research Letters, 2021, 92, 2961-2971.	1.9	17
22	The long-term observation in Chinese children with monocular myelinated retinal nerve fibers, myopia and amblyopia. Translational Pediatrics, 2021, 10, 860-869.	1.2	0
23	Long-range transport of ozone across the eastern China seas: A case study in coastal cities in southeastern China. Science of the Total Environment, 2021, 768, 144520.	8.0	34
24	Glucose Decoration on Wall Teichoic Acid Is Required for Phage Adsorption and InlB-Mediated Virulence in Listeria ivanovii. Journal of Bacteriology, 2021, 203, e0013621.	2.2	2
25	One-Year Follow-Up of Corneal Biomechanical Changes After Accelerated Transepithelial Corneal Cross-Linking in Pediatric Patients With Progressive Keratoconus. Frontiers in Medicine, 2021, 8, 663494.	2.6	3
26	Designing polymer nanocomposites with high energy density using machine learning. Npj Computational Materials, 2021, 7, .	8.7	39
27	ICAM1 initiates CTC cluster formation and trans-endothelial migration in lung metastasis of breast cancer. Nature Communications, 2021, 12, 4867.	12.8	97
28	Effects of warm compress on tear film, blink pattern and Meibomian gland function in dry eyes after corneal refractive surgery. BMC Ophthalmology, 2021, 21, 330.	1.4	9
29	The Driving Influence of Multi-Dimensional Urbanization on PM2.5 Concentrations in Africa: New Evidence from Multi-Source Remote Sensing Data, 2000–2018. International Journal of Environmental Research and Public Health, 2021, 18, 9389.	2.6	20
30	Comparison of Corneal Biomechanics in Post-SMILE, Post-LASEK, and Keratoconic Eyes. Frontiers in Medicine, 2021, 8, 695697.	2.6	8
31	A Survey on Al-Driven Digital Twins in Industry 4.0: Smart Manufacturing and Advanced Robotics. Sensors, 2021, 21, 6340.	3.8	95
32	Core-shell hybrid pre-preg tow for lightweight composite truss. Composites Part B: Engineering, 2021, 223, 109093.	12.0	1
33	Delineating the spatial-temporal variation of air pollution with urbanization in the Belt and Road Initiative area. Environmental Impact Assessment Review, 2021, 91, 106646.	9.2	68
34	Robots Under COVID-19 Pandemic: A Comprehensive Survey. IEEE Access, 2021, 9, 1590-1615.	4.2	149
35	Bacillus subtilis YngB contributes to wall teichoic acid glucosylation and glycolipid formation during anaerobic growth. Journal of Biological Chemistry, 2021, 296, 100384.	3.4	10
36	Femtosecond Laser-Assisted Small Incision Allogeneic Endokeratophakia Using a Hyperopic Lenticule in Rabbits. Translational Vision Science and Technology, 2021, 10, 29.	2.2	1

#	Article	IF	CITATIONS
37	Light-mediated discovery of surfaceome nanoscale organization and intercellular receptor interaction networks. Nature Communications, 2021, 12, 7036.	12.8	33
38	Long-Term Follow-Up of Accelerated Transepithelial Corneal Crosslinking for Post-LASIK Ectasia: A Pilot Prospective Observational Study. Frontiers in Bioengineering and Biotechnology, 2021, 9, 809262.	4.1	3
39	Orientation optimization in anisotropic materials using gradient descent method. Composite Structures, 2020, 234, 111680.	5.8	11
40	Object-Based Mapping of Plastic Greenhouses with Scattered Distribution in Complex Land Cover Using Landsat 8 OLI Images: A Case Study in Xuzhou, China. Journal of the Indian Society of Remote Sensing, 2020, 48, 287-303.	2.4	15
41	Stathmin 1 Induces Murine Hepatocyte Proliferation and Increased Liver Mass. Hepatology Communications, 2020, 4, 38-49.	4.3	8
42	Visual Outcomes after Small Incision Lenticule Extraction and Femtosecond Laser-Assisted LASIK for High Myopia. Ophthalmic Research, 2020, 63, 427-433.	1.9	8
43	Upper Limb Exoskeleton Systems—Overview. , 2020, , 1-22.		12
44	EXO-UL Upper Limb Robotic Exoskeleton System Series: From 1 DOF Single-Arm to (7+1) DOFs Dual-Arm. , 2020, , 91-103.		1
45	Hand Exoskeleton Systems—Overview. , 2020, , 149-175.		14
46	NO _{<i>x</i>} Emission Changes Over China During the COVIDâ€19 Epidemic Inferred From Surface NO ₂ Observations. Geophysical Research Letters, 2020, 47, e2020GL090080.	4.0	62
47	Significantly increased energy density and discharge efficiency at high temperature in polyetherimide nanocomposites by a small amount of Al ₂ O ₃ nanoparticles. Journal of Materials Chemistry A, 2020, 8, 24536-24542.	10.3	98
48	Network-principled deep generative models for designing drug combinations as graph sets. Bioinformatics, 2020, 36, i445-i454.	4.1	24
49	Topologically distributed one-dimensional TiO ₂ nanofillers maximize the dielectric energy density in a P(VDF-HFP) nanocomposite. Journal of Materials Chemistry A, 2020, 8, 18244-18253.	10.3	18
50	Hybrid Humanoid Robotic Head Mechanism: Design, Modeling, and Experiments with Object Tracking. , 2020, , .		2
51	De Novo Protein Design for Novel Folds Using Guided Conditional Wasserstein Generative Adversarial Networks. Journal of Chemical Information and Modeling, 2020, 60, 5667-5681.	5.4	44
52	Corneal Densitometry After Small Incision Lenticule Extraction (SMILE) and Femtosecond Laser-Assisted LASIK (FS-LASIK): 5-Year Prospective Comparative Study. Frontiers in Medicine, 2020, 7, 521078.	2.6	10
53	Modeling the Effects of Global and Diffuse Radiation on Terrestrial Gross Primary Productivity in China Based on a Two-Leaf Light Use Efficiency Model. Remote Sensing, 2020, 12, 3355.	4.0	12
54	Glycotyping and Specific Separation of Listeria monocytogenes with a Novel Bacteriophage Protein Tool Kit. Applied and Environmental Microbiology, 2020, 86, .	3.1	31

#	Article	IF	CITATIONS
55	Colossal thermoelectric enhancement in Cu _{2+x} Zn _{1â^'x} SnS ₄ solid solution by local disordering of crystal lattice and multi-scale defect engineering. Journal of Materials Chemistry A, 2020, 8, 10909-10916.	10.3	27
56	Detecting Slow Slip Events From Seafloor Pressure Data Using Machine Learning. Geophysical Research Letters, 2020, 47, e2020GL087579.	4.0	10
57	An Allâ€5cale Hierarchical Architecture Induces Colossal Roomâ€Temperature Electrocaloric Effect at Ultralow Electric Field in Polymer Nanocomposites. Advanced Materials, 2020, 32, e1907927.	21.0	34
58	Bayesian Active Learning for Optimization and Uncertainty Quantification in Protein Docking. Journal of Chemical Theory and Computation, 2020, 16, 5334-5347.	5.3	12
59	Energyâ€based graph convolutional networks for scoring protein docking models. Proteins: Structure, Function and Bioinformatics, 2020, 88, 1091-1099.	2.6	40
60	Blow-spun N-doped carbon fiber based high performance flexible lithium ion capacitors. RSC Advances, 2020, 10, 9833-9839.	3.6	3
61	Galactosylated wall teichoic acid, but not lipoteichoic acid, retains InIB on the surface of serovar 4b <i>Listeria monocytogenes</i> . Molecular Microbiology, 2020, 113, 638-649.	2.5	17
62	Accelerated (45 mW/cm2) Transepithelial Corneal Cross-Linking for Progressive Keratoconus Patients: Long-Term Topographical and Clinical Outcomes. Frontiers in Medicine, 2020, 7, 283.	2.6	10
63	An alternating multilayer architecture boosts ultrahigh energy density and high discharge efficiency in polymer composites. RSC Advances, 2020, 10, 5886-5893.	3.6	19
64	The distribution and drivers of PM2.5 in a rapidly urbanizing region: The Belt and Road Initiative in focus. Science of the Total Environment, 2020, 716, 137010.	8.0	57
65	Structure and function of <i>Listeria</i> teichoic acids and their implications. Molecular Microbiology, 2020, 113, 627-637.	2.5	37
66	Extracellular Domains I and II of cell-surface glycoprotein CD44 mediate its trans-homophilic dimerization and tumor cluster aggregation. Journal of Biological Chemistry, 2020, 295, 2640-2649.	3.4	24
67	Two-year observation of morphologic and histopathologic changes in the monkey cornea following small incision allogenic lenticule implantation. Experimental Eye Research, 2020, 192, 107935.	2.6	7
68	Tracking national sustainability of critical natural capital and the socioeconomic drivers in the context of the Belt and Road Initiative. Ecological Indicators, 2020, 114, 106315.	6.3	16
69	Earlyâ€Stage Lithospheric Foundering Beneath the Eastern Tibetan Plateau Revealed by Fullâ€Wave <i>P</i> _n Tomography. Geophysical Research Letters, 2020, 47, e2019GL086469.	4.0	9
70	Small Incision Lenticule Extraction (SMILE) for Moderate and High Myopia: Seven-Year Outcomes of Refraction, Corneal Tomography, and Wavefront Aberrations. Journal of Ophthalmology, 2020, 2020, 1-7.	1.3	18
71	Management of Suction Loss During SMILE in 12,057 Eyes: Incidence, Outcomes, Risk Factors, and a Novel Method of Same-Day Recutting of Refractive Lenticules. Journal of Refractive Surgery, 2020, 36, 308-316.	2.3	6
72	Planar multi-angle retro-reflectors based on the wave-vector-reversion of spoof surface plasmon polaritons. Optics Express, 2020, 28, 37236.	3.4	1

#	Article	IF	CITATIONS
73	Modeling Threeâ€Dimensional Wave Propagation in Anelastic Models With Surface Topography by the Optimal Strong Stability Preserving Rungeâ€Kutta Method. Journal of Geophysical Research: Solid Earth, 2019, 124, 890-907.	3.4	9
74	Locating Shallow Seismic Sources With Waves Scattered by Surface Topography: Validation of the Method at the Nevada Test Site. Journal of Geophysical Research: Solid Earth, 2019, 124, 7040-7051.	3.4	0
75	Lace Braiding Machines for Composite Preform Manufacture. , 2019, , .		1
76	High-performance Li ₆ PS ₅ Cl-based all-solid-state lithium-ion batteries. Journal of Materials Chemistry A, 2019, 7, 18612-18618.	10.3	40
77	Relationship Among Corneal Stiffness, Thickness, and Biomechanical Parameters Measured by Corvis ST, Pentacam and ORA in Keratoconus. Frontiers in Physiology, 2019, 10, 740.	2.8	39
78	Phage resistance at the cost of virulence: Listeria monocytogenes serovar 4b requires galactosylated teichoic acids for InlB-mediated invasion. PLoS Pathogens, 2019, 15, e1008032.	4.7	78
79	A Ferroconcreteâ€Like Allâ€Organic Nanocomposite Exhibiting Improved Mechanical Property, High Breakdown Strength, and High Energy Efficiency. Macromolecular Materials and Engineering, 2019, 304, 1900433.	3.6	17
80	Effect of joint stiffness on torsional stiffness of open lattice composite structures. Journal of Industrial Textiles, 2019, , 152808371988181.	2.4	2
81	An in Situ-Formed Mosaic Li ₇ Sn ₃ /LiF Interface Layer for High-Rate and Long-Life Garnet-Based Lithium Metal Batteries. ACS Applied Materials & Interfaces, 2019, 11, 34939-34947.	8.0	66
82	Admittance Control Scheme Comparison of EXO-UL8: A Dual-Arm Exoskeleton Robotic System. , 2019, 2019, 611-617.		10
83	A hybrid sub-lineage of Listeria monocytogenes comprising hypervirulent isolates. Nature Communications, 2019, 10, 4283.	12.8	76
84	Evaluating the predictions of the protein stability change upon single amino acid substitutions for the FXN CAGI5 challenge. Human Mutation, 2019, 40, 1392-1399.	2.5	16
85	Mechanical analysis of the auxetic behavior of novel braided tubular structures by the finite element method. Textile Reseach Journal, 2019, 89, 5187-5197.	2.2	8
86	Predicting pathogenicity of missense variants with weakly supervised regression. Human Mutation, 2019, 40, 1579-1592.	2.5	5
87	Correlation Between Corneal Topographic, Densitometry, and Biomechanical Parameters in Keratoconus Eyes. Translational Vision Science and Technology, 2019, 8, 12.	2.2	39
88	Non-intuitive concomitant enhancement of dielectric permittivity, breakdown strength and energy density in percolative polymer nanocomposites by trace Ag nanodots. Journal of Materials Chemistry A, 2019, 7, 15198-15206.	10.3	61
89	Engineering a HER2-specific antibody–drug conjugate to increase lysosomal delivery and therapeutic efficacy. Nature Biotechnology, 2019, 37, 523-526.	17.5	58
90	Overcoming the Pixel-Density Limit in Plasmonic Absorbing Structure for Broadband Absorption Enhancement. IEEE Antennas and Wireless Propagation Letters, 2019, 18, 674-678.	4.0	6

#	Article	IF	CITATIONS
91	Polymer Nanocomposites with Interpenetrating Gradient Structure Exhibiting Ultrahigh Discharge Efficiency and Energy Density. Advanced Energy Materials, 2019, 9, 1803411.	19.5	132
92	Initial rupture processes of the 2008 Mw7.9 Wenchuan, China earthquake: From near-source seismic records. Journal of Asian Earth Sciences, 2019, 173, 397-403.	2.3	5
93	Enhanced electrocaloric strength of P(VDF-TrFE-CFE) induced by edge-on lamellae. Journal of Materials Chemistry C, 2019, 7, 3212-3217.	5.5	11
94	DeepAffinity: interpretable deep learning of compound–protein affinity through unified recurrent and convolutional neural networks. Bioinformatics, 2019, 35, 3329-3338.	4.1	279
95	Modulating interfacial charge distribution and compatibility boosts high energy density and discharge efficiency of polymer nanocomposites. RSC Advances, 2019, 9, 35990-35997.	3.6	12
96	Upper Mantle Earth Structure in Africa From Fullâ€Wave Ambient Noise Tomography. Geochemistry, Geophysics, Geosystems, 2019, 20, 120-147.	2.5	55
97	Spatiotemporal patterns of recent PM2.5 concentrations over typical urban agglomerations in China. Science of the Total Environment, 2019, 655, 13-26.	8.0	112
98	Synthetical dispersion engineering in plasmonic metamaterial absorber for broadband absorption enhancement. Journal Physics D: Applied Physics, 2019, 52, 085103.	2.8	15
99	Multistage dispersion engineering in a three-dimensional plasmonic structure for outstanding broadband absorption. Optical Materials Express, 2019, 9, 1539.	3.0	8
100	Design of a Hand Exoskeleton for Use with Upper Limb Exoskeletons. Biosystems and Biorobotics, 2019, , 276-280.	0.3	7
101	High Capacity and Superior Cyclic Performances of All-Solid-State Lithium Batteries Enabled by a Glass–Ceramics Solo. ACS Applied Materials & Interfaces, 2018, 10, 10029-10035.	8.0	37
102	Water-based metamaterial absorbers for optical transparency and broadband microwave absorption. Journal of Applied Physics, 2018, 123, .	2.5	81
103	Genomic and Molecular Landscape of DNA Damage Repair Deficiency across The Cancer Genome Atlas. Cell Reports, 2018, 23, 239-254.e6.	6.4	801
104	Threeâ€Dimensional Passiveâ€Source Reverseâ€Time Migration of Converted Waves: The Method. Journal of Geophysical Research: Solid Earth, 2018, 123, 1419-1434.	3.4	14
105	One-year follow-up of accelerated transepithelial corneal collagen cross-linking for progressive pediatric keratoconus. BMC Ophthalmology, 2018, 18, 75.	1.4	25
106	Asymmetric Dual Arm Approach For Post Stroke Recovery Of Motor Functions Utilizing The EXO-UL8 Exoskeleton System: A Pilot Study. , 2018, 2018, 1701-1707.		16
107	Two-year topographic and densitometric outcomes of accelerated (45 mW/cm2) transepithelial corneal cross-linking for keratoconus: a case-control study. BMC Ophthalmology, 2018, 18, 337.	1.4	9
108	High-performance all-solid-state lithium–sulfur batteries with sulfur/carbon nano-hybrids in a composite cathode. Journal of Materials Chemistry A, 2018, 6, 23345-23356.	10.3	48

#	Article	lF	CITATIONS
109	Transparent absorption-diffusion-integrated water-based all-dielectric metasurface for broadband backward scattering reduction. Journal Physics D: Applied Physics, 2018, 51, 485301.	2.8	19
110	Transparent and broadband absorption-diffusion-integrated low-scattering metamaterial by standing-up lattice. Optics Express, 2018, 26, 28363.	3.4	27
111	iCFN: an efficient exact algorithm for multistate protein design. Bioinformatics, 2018, 34, i811-i820.	4.1	18
112	Broadband radar absorbing sandwich structures with enhanced mechanical properties. Results in Physics, 2018, 11, 253-258.	4.1	13
113	Seismic evidence for significant melt beneath the Long Valley Caldera, California, USA. Geology, 2018, 46, 799-802.	4.4	42
114	Fullâ€Waveform Sensitivity Kernels of Componentâ€Differential Traveltimes and ZH Amplitude Ratios for Velocity and Density Tomography. Journal of Geophysical Research: Solid Earth, 2018, 123, 4829-4840.	3.4	9
115	Conventional and transepithelial corneal cross-linking for patients with keratoconus. PLoS ONE, 2018, 13, e0195105.	2.5	22
116	Lithium-Salt-Rich PEO/Li _{0.3} La _{0.557} TiO ₃ Interpenetrating Composite Electrolyte with Three-Dimensional Ceramic Nano-Backbone for All-Solid-State Lithium-Ion Batteries. ACS Applied Materials & Interfaces, 2018, 10, 24791-24798.	8.0	230
117	Tailoring multi-order absorptions of a Salisbury screen based on dispersion engineering of spoof surface plasmon polariton. Journal Physics D: Applied Physics, 2018, 51, 315103.	2.8	11
118	Upper Limb Wearable Exoskeleton Systems for Rehabilitation. , 2018, , 71-90.		5
119	Transparent broadband metamaterial absorber enhanced by water-substrate incorporation. Optics Express, 2018, 26, 15665.	3.4	99
120	Three-Dimensional Resistive Metamaterial Absorber Loaded with Metallic Resonators for the Enhancement of Lower-Frequency Absorption. Materials, 2018, 11, 210.	2.9	14
121	Long-Term Analysis of Aerosol Optical Depth over the Huaihai Economic Region (HER): Possible Causes and Implications. Atmosphere, 2018, 9, 93.	2.3	8
122	A general approach to fast prototype the topology of braided structures. International Journal of Engineering Science, 2018, 131, 40-60.	5.0	9
123	Addressing the Interface Issues in All-Solid-State Bulk-Type Lithium Ion Battery via an All-Composite Approach. ACS Applied Materials & Interfaces, 2017, 9, 9654-9661.	8.0	139
124	Wave speed structure of the eastern North American margin. Earth and Planetary Science Letters, 2017, 459, 394-405.	4.4	37
125	c-Myc promotes renal fibrosis by inducing integrin αv-mediated transforming growth factor-β signaling. Kidney International, 2017, 92, 888-899.	5.2	52
126	Structural and functional diversity in Listeria cell wall teichoic acids. Journal of Biological Chemistry, 2017, 292, 17832-17844.	3.4	55

#	Article	IF	CITATIONS
127	Growth of the northeastern margin of the Tibetan Plateau by squeezing up of the crust at the boundaries. Scientific Reports, 2017, 7, 10591.	3.3	11
128	Synergistic Coupling between Li _{6.75} La ₃ Zr _{1.75} Ta _{0.25} O ₁₂ and Poly(vinylidene fluoride) Induces High Ionic Conductivity, Mechanical Strength, and Thermal Stability of Solid Composite Electrolytes. Journal of the American Chemical Society, 2017, 139, 13779-13785.	13.7	698
129	Broadband reflectionless metamaterials with customizable absorption–transmission-integrated performance. Applied Physics A: Materials Science and Processing, 2017, 123, 1.	2.3	22
130	High Capacity, Superior Cyclic Performances in All-Solid-State Lithium-Ion Batteries Based on 78Li ₂ S-22P ₂ S ₅ Glass-Ceramic Electrolytes Prepared via Simple Heat Treatment. ACS Applied Materials & Interfaces, 2017, 9, 28542-28548.	8.0	49
131	Corneal Lenticule Allotransplantation After Femtosecond Laser Small Incision Lenticule Extraction in Rabbits. Cornea, 2017, 36, 222-228.	1.7	25
132	Tuning Phase Composition of Polymer Nanocomposites toward High Energy Density and High Discharge Efficiency by Nonequilibrium Processing. ACS Applied Materials & Interfaces, 2017, 9, 29717-29731.	8.0	81
133	Seismic evidence for a possible deep crustal hot zone beneath Southwest Washington. Scientific Reports, 2017, 7, 7400.	3.3	25
134	Predicting protein conformational changes for unbound and homology docking: learning from intrinsic and induced flexibility. Proteins: Structure, Function and Bioinformatics, 2017, 85, 544-556.	2.6	12
135	Upper limb redundancy resolution under gravitational loading conditions: Arm postural stability index based on dynamic manipulability analysis. , 2017, , .		7
136	Modeling of joint synergy and spasticity in stroke patients to solve arm reach tasks. , 2017, , .		3
137	A Cost-Effective Geodetic Strainmeter Based on Dual Coaxial Cable Bragg Gratings. Sensors, 2017, 17, 842.	3.8	11
138	Biomechanical and Histopathologic Effects of Pulsed-Light Accelerated Epithelium-On/-Off Corneal Collagen Cross-Linking. Cornea, 2017, 36, 854-859.	1.7	4
139	A Three-Year Observation of Corneal Backscatter After Small Incision Lenticule Extraction (SMILE). Journal of Refractive Surgery, 2017, 33, 377-382.	2.3	16
140	Metformin Prevents Renal Fibrosis in Mice with Unilateral Ureteral Obstruction and Inhibits Ang II-Induced ECM Production in Renal Fibroblasts. International Journal of Molecular Sciences, 2016, 17, 146.	4.1	44
141	Prediction of homoprotein and heteroprotein complexes by protein docking and templateâ€based modeling: A CASPâ€CAPRI experiment. Proteins: Structure, Function and Bioinformatics, 2016, 84, 323-348.	2.6	148
142	Accurate source location from waves scattered by surface topography. Journal of Geophysical Research: Solid Earth, 2016, 121, 4538-4552.	3.4	6
143	Changes in intraocular pressure values measured with noncontact tonometer (NCT), ocular response analyzer (ORA) and corvis scheimpflug technology tonometer (CST) in the early phase after small incision lenticule extraction (SMILE). BMC Ophthalmology, 2016, 16, 205.	1.4	13
144	Assessing waveform predictions of recent threeâ€dimensional velocity models of the Tibetan Plateau. Journal of Geophysical Research: Solid Earth, 2016, 121, 2521-2538.	3.4	5

#	Article	IF	CITATIONS
145	N-acetylcysteine alleviates angiotensin II-mediated renal fibrosis in mouse obstructed kidneys. Acta Pharmacologica Sinica, 2016, 37, 637-644.	6.1	36
146	Imaging Rayleigh wave attenuation with USArray. Geophysical Journal International, 2016, 206, 241-259.	2.4	27
147	Identification of YbeY-Protein Interactions Involved in 16S rRNA Maturation and Stress Regulation in Escherichia coli. MBio, 2016, 7, .	4.1	51
148	Location and moment tensor inversion of small earthquakes using 3D Green's functions in models with rugged topography: application to the Longmenshan fault zone. Earthquake Science, 2016, 29, 139-151.	0.9	5
149	One-Year Follow-Up of Changes in Corneal Densitometry After Accelerated (45 mW/cm2) Transepithelial Corneal Collagen Cross-Linking for Keratoconus. Cornea, 2016, 35, 1434-1440.	1.7	38
150	Insulin deficiency induces rat renal mesangial cell dysfunction via activation of IGF-1/IGF-1R pathway. Acta Pharmacologica Sinica, 2016, 37, 217-227.	6.1	21
151	Crustal and upper mantle structure beneath the northeastern Tibetan Plateau from joint analysis of receiver functions and Rayleigh wave dispersions. Geophysical Journal International, 2016, 204, 583-590.	2.4	29
152	A Pilot Study of SMILE for Hyperopia: Corneal Morphology and Surface Characteristics of Concave Lenticules in Human Donor Eyes. Journal of Refractive Surgery, 2016, 32, 713-716.	2.3	9
153	Using Donor Lenticules Obtained Through SMILE for an Epikeratophakia Technique Combined With Phototherapeutic Keratectomy. Journal of Refractive Surgery, 2016, 32, 840-845.	2.3	22
154	Validation of recent shear wave velocity models in the United States with fullâ€wave simulation. Journal of Geophysical Research: Solid Earth, 2015, 120, 344-358.	3.4	13
155	Diffuse lamellar keratitis after small-incision lenticule extraction. Journal of Cataract and Refractive Surgery, 2015, 41, 400-407.	1.5	47
156	Finite element analysis of monofilament woven fabrics under uniaxial tension. Journal of the Textile Institute, 2015, 106, 90-100.	1.9	10
157	Seismic wave speed structure of the Ontong Java Plateau. Earth and Planetary Science Letters, 2015, 420, 140-150.	4.4	31
158	Effects of seasonal changes in ambient noise sources on monitoring temporal variations in crustal properties. Journal of Seismology, 2015, 19, 781-790.	1.3	4
159	CHOP mediates XBP1S-induced renal mesangial cell necrosis following high glucose treatment. European Journal of Pharmacology, 2015, 758, 89-96.	3.5	16
160	A Preliminary Fullâ€Wave Ambientâ€Noise Tomography Model Spanning from the Juan de Fuca and Gorda Spreading Centers to the Cascadia Volcanic Arc. Seismological Research Letters, 2015, 86, 1253-1260.	1.9	20
161	Towards aspirin-inspired self-immolating molecules which target the cyclooxygenases. Organic and Biomolecular Chemistry, 2015, 13, 11078-11086.	2.8	0
162	Molecular mechanisms and design principles for promiscuous inhibitors to avoid drug resistance: Lessons learned from HIV â€1 protease inhibition. Proteins: Structure, Function and Bioinformatics, 2015, 83, 351-372.	2.6	9

#	Article	IF	CITATIONS
163	Intra- and Intersession Repeatability of an Optical Quality and Intraocular Scattering Measurement System in Children. PLoS ONE, 2015, 10, e0142189.	2.5	15
164	The Safety and Predictability of Implanting Autologous Lenticule Obtained by SMILE for Hyperopia. Journal of Refractive Surgery, 2015, 31, 374-379.	2.3	104
165	Mild Decentration Measured by a Scheimpflug Camera and Its Impact on Visual Quality Following SMILE in the Early Learning Curve. , 2014, 55, 3886.		104
166	Changes in Corneal Deformation Parameters after Lenticule Creation and Extraction during Small Incision Lenticule Extraction (SMILE) Procedure. PLoS ONE, 2014, 9, e103893.	2.5	28
167	P300-dependent STAT3 acetylation is necessary for angiotensin II-induced pro-fibrotic responses in renal tubular epithelial cells. Acta Pharmacologica Sinica, 2014, 35, 1157-1166.	6.1	31
168	Crustal Velocity Structure of the Northeastern Tibetan Plateau from Ambient Noise Surface-Wave Tomography and Its Tectonic Implications. Bulletin of the Seismological Society of America, 2014, 104, 1045-1055.	2.3	12
169	Comparison of Corneal Deformation Parameters After SMILE, LASEK, and Femtosecond Laser-Assisted LASIK. Journal of Refractive Surgery, 2014, 30, 310-318.	2.3	93
170	The distribution of the midâ€ŧoâ€lower crustal lowâ€velocity zone beneath the northeastern Tibetan Plateau revealed from ambient noise tomography. Journal of Geophysical Research: Solid Earth, 2014, 119, 1954-1970.	3.4	97
171	Inhibition of STAT3 acetylation is associated with attenuated renal fibrosis in the obstructed kidney. Acta Pharmacologica Sinica, 2014, 35, 1045-1054.	6.1	27
172	Blind prediction of interfacial water positions in CAPRI. Proteins: Structure, Function and Bioinformatics, 2014, 82, 620-632.	2.6	50
173	Upper mantle structure of the Cascades from full-wave ambient noise tomography: Evidence for 3D mantle upwelling in the back-arc. Earth and Planetary Science Letters, 2014, 390, 222-233.	4.4	73
174	Mesoscale convective system surface pressure anomalies responsible for meteotsunamis along the U.S. East Coast on June 13th, 2013. Scientific Reports, 2014, 4, 7143.	3.3	39
175	Comparison of Corneal Sensation Between Small Incision Lenticule Extraction (SMILE) and Femtosecond Laser-Assisted LASIK for Myopia. Journal of Refractive Surgery, 2014, 30, 94-100.	2.3	52
176	Optical Quality and Intraocular Scattering After Femtosecond Laser Small Incision Lenticule Extraction. Journal of Refractive Surgery, 2014, 30, 296-302.	2.3	48
177	ESR1 ligand-binding domain mutations in hormone-resistant breast cancer. Nature Genetics, 2013, 45, 1439-1445.	21.4	960
178	Diffuse lamellar keratitis after femtosecond laser refractive lenticule extraction. JCRS Online Case Reports, 2013, 1, e26-e32.	0.2	0
179	Three-dimensional quantitative in situ study of crack initiation and propagation in AA6061 aluminum alloy sheets via synchrotron laminography and finite-element simulations. Acta Materialia, 2013, 61, 2571-2582.	7.9	66
180	Theoretical Graetz–Damköhler modeling of an air-breathing microfluidic fuel cell. Journal of Power Sources, 2013, 231, 1-5.	7.8	22

#	Article	IF	CITATIONS
181	Elevated transcriptional co-activator p102 mediates angiotensin II type 1 receptor up-regulation and extracellular matrix overproduction in the high glucose-treated rat glomerular mesangial cells and isolated glomeruli. European Journal of Pharmacology, 2013, 702, 208-217.	3.5	11
182	Testing the Substrate-Envelope Hypothesis with Designed Pairs of Compounds. ACS Chemical Biology, 2013, 8, 2433-2441.	3.4	33
183	Improved flexible refinement of protein docking in CAPRI rounds 22–27. Proteins: Structure, Function and Bioinformatics, 2013, 81, 2129-2136.	2.6	17
184	Shear wave structure in the northeastern Tibetan Plateau from Rayleigh wave tomography. Journal of Geophysical Research: Solid Earth, 2013, 118, 4170-4183.	3.4	34
185	Suppression of XBP1S Mediates High Glucose-Induced Oxidative Stress and Extracellular Matrix Synthesis in Renal Mesangial Cell and Kidney of Diabetic Rats. PLoS ONE, 2013, 8, e56124.	2.5	29
186	The Morphology of Corneal Cap and Its Relation to Refractive Outcomes in Femtosecond Laser Small Incision Lenticule Extraction (SMILE) with Anterior Segment Optical Coherence Tomography Observation. PLoS ONE, 2013, 8, e70208.	2.5	37
187	H2S Inhibits Hyperglycemia-Induced Intrarenal Renin-Angiotensin System Activation via Attenuation of Reactive Oxygen Species Generation. PLoS ONE, 2013, 8, e74366.	2.5	68
188	Comparison of Dry Eye and Corneal Sensitivity between Small Incision Lenticule Extraction and Femtosecond LASIK for Myopia. PLoS ONE, 2013, 8, e77797.	2.5	106
189	Overcoming mutation-based resistance to antiandrogens with rational drug design. ELife, 2013, 2, e00499.	6.0	334
190	Microdistortions in Bowman's Layer Following Femtosecond Laser Small Incision Lenticule Extraction Observed by Fourier-Domain OCT. Journal of Refractive Surgery, 2013, 29, 668-674.	2.3	64
191	An Improved Method to Extract Very-Broadband Empirical Green's Functions from Ambient Seismic Noise. Bulletin of the Seismological Society of America, 2012, 102, 1872-1877.	2.3	65
192	Charge Optimization Theory for Induced-Fit Ligands. Journal of Chemical Theory and Computation, 2012, 8, 4580-4592.	5.3	8
193	Validation of Shear-Wave Velocity Models of the Pacific Northwest. Bulletin of the Seismological Society of America, 2012, 102, 2611-2621.	2.3	20
194	A complex Tibetan upper mantle: A fragmented Indian slab and no south-verging subduction of Eurasian lithosphere. Earth and Planetary Science Letters, 2012, 333-334, 101-111.	4.4	117
195	Upper mantle structures beneath the Carpathian–Pannonian region: Implications for the geodynamics of continental collision. Earth and Planetary Science Letters, 2012, 349-350, 139-152.	4.4	66
196	Azimuthal anisotropy of <i>Lg</i> attenuation in eastern Tibetan Plateau. Journal of Geophysical Research, 2012, 117, .	3.3	13
197	Three-dimensional anisotropic seismic wave modelling in spherical coordinates by a collocated-grid finite-difference method. Geophysical Journal International, 2012, 188, 1359-1381.	2.4	66
198	Crustal and mantle velocity models of southern Tibet from finite frequency tomography. Journal of Geophysical Research, 2011, 116, .	3.3	28

#	Article	IF	CITATIONS
199	High resolution regional seismic attenuation tomography in eastern Tibetan Plateau and adjacent regions. Geophysical Research Letters, 2011, 38, n/a-n/a.	4.0	43
200	Experimental and numerical characterization of anisotropic damage evolution of forged Al6061-T6 alloy. Procedia Engineering, 2011, 10, 3429-3434.	1.2	12
201	Achieving reliability and high accuracy in automated protein docking: Cluspro, PIPER, SDU, and stability analysis in CAPRI rounds 13–19. Proteins: Structure, Function and Bioinformatics, 2010, 78, 3124-3130.	2.6	211
202	Unsplit complex frequency-shifted PML implementation using auxiliary differential equations for seismic wave modeling. Geophysics, 2010, 75, T141-T154.	2.6	168
203	Seismic evidence for a Moho offset and south-directed thrust at the easternmost Qaidam–Kunlun boundary in the Northeast Tibetan plateau. Earth and Planetary Science Letters, 2009, 288, 329-334.	4.4	67
204	Numerical simulation of strong ground motion for the M s8.0 Wenchuan earthquake of 12 May 2008. Science in China Series D: Earth Sciences, 2008, 51, 1673-1682.	0.9	41
205	Cross-dependence of finite-frequency compressional waveforms to shear seismic wave speeds. Geophysical Journal International, 2008, 174, 941-948.	2.4	21
206	Finite frequency tomography in southeastern Tibet: Evidence for the causal relationship between mantle lithosphere delamination and the north–south trending rifts. Journal of Geophysical Research, 2008, 113, .	3.3	71
207	Component-Dependent Frechet Sensitivity Kernels and Utility of Three-Component Seismic Records. Bulletin of the Seismological Society of America, 2008, 98, 2517-2525.	2.3	4
208	Protein Docking by the Underestimation of Free Energy Funnels in the Space of Encounter Complexes. PLoS Computational Biology, 2008, 4, e1000191.	3.2	41
209	SDU: A Semidefinite Programming-Based Underestimation Method for Stochastic Global Optimization in Protein Docking. IEEE Transactions on Automatic Control, 2007, 52, 664-676.	5.7	20
210	Docking with PIPER and refinement with SDU in rounds 6–11 of CAPRI. Proteins: Structure, Function and Bioinformatics, 2007, 69, 734-742.	2.6	12
211	ClusPro: Performance in CAPRI rounds 6–11 and the new server. Proteins: Structure, Function and Bioinformatics, 2007, 69, 781-785.	2.6	77
212	Finite-frequency sensitivity kernels for head waves. Geophysical Journal International, 2007, 171, 847-856.	2.4	29
213	Upper mantle structure beneath the Azores hotspot from finite-frequency seismic tomography. Earth and Planetary Science Letters, 2006, 250, 11-26.	4.4	116
214	Frequency-Dependent Crustal Correction for Finite-Frequency Seismic Tomography. Bulletin of the Seismological Society of America, 2006, 96, 2441-2448.	2.3	18
215	P-wave velocity structure of the crust and uppermost mantle beneath Iceland from local earthquake tomography. Earth and Planetary Science Letters, 2005, 235, 597-609.	4.4	11
216	Imaging seismic velocity structure beneath the Iceland hot spot: A finite frequency approach. Journal of Geophysical Research, 2004, 109, .	3.3	109

#	Article	IF	CITATIONS
217	Thermal, hydrous, and mechanical states of the mantle transition zone beneath southern Africa. Earth and Planetary Science Letters, 2004, 217, 367-378.	4.4	39
218	Coupled seismic slip on adjacent oceanic transform faults. Geophysical Research Letters, 2003, 30, .	4.0	16
219	Seismic evidence for accumulated oceanic crust above the 660-km discontinuity beneath southern Africa. Geophysical Research Letters, 2003, 30, .	4.0	44
220	Seismological evidence for a mid-mantle discontinuity beneath Hawaii and Iceland. Earth and Planetary Science Letters, 2003, 214, 143-151.	4.4	36
221	Seismic evidence for a tilted mantle plume and north–south mantle flow beneath Iceland. Earth and Planetary Science Letters, 2002, 197, 261-272.	4.4	76
222	Mantle flow, melting, and dehydration of the Iceland mantle plume. Earth and Planetary Science Letters, 1999, 165, 81-96.	4.4	172
223	Seismic evidence for a lower-mantle origin of the Iceland plume. Nature, 1998, 395, 62-65.	27.8	214
224	Mantle Discontinuity Structure Beneath the Southern East Pacific Rise from P-to-S Converted Phases. Science, 1998, 280, 1232-1235.	12.6	61
225	Phase Velocities of Rayleigh Waves in the MELT Experiment on the East Pacific Rise. Science, 1998, 280, 1235-1238.	12.6	197
226	Investigation of microearthquake activity following an intraplate teleseismic swarm on the west flank of the Southern East Pacific Rise. Journal of Geophysical Research, 1997, 102, 459-475.	3.3	30
227	Hot mantle transition zone beneath Iceland and the adjacent Mid-Atlantic Ridge inferred from P-to-S conversions at the 410- and 660-km discontinuities. Geophysical Research Letters, 1996, 23, 3527-3530.	4.0	43
228	Abundant seamounts of the Rano Rahi seamount field near the Southern East Pacific Rise, 15� S to 19� S. Marine Geophysical Researches, 1996, 18, 13-52.	1.2	55
229	Trade-off in production between adjacent seamount chains near the East Pacific Rise. Nature, 1995, 373, 140-143.	27.8	39
230	Geochemical constraints on initial and final depths of melting beneath mid-ocean ridges. Journal of Geophysical Research, 1995, 100, 2211-2237.	3.3	216
231	A Method to Measure Effective Flexural and Transverse Shear Modulus of Composite Structures with Large Aspect Ratio. Experimental Mechanics, 0, , 1.	2.0	0